


## Thermal Transparency Induced by Periodic Interparticle Interaction

Liujuan Xu, Shuai Yang, and Jiping Huang\*

*Department of Physics, State Key Laboratory of Surface Physics, and Key Laboratory of Micro and Nano Photonic Structures (MOE), Fudan University, 200433 Shanghai, China*

 (Received 11 January 2019; revised manuscript received 4 March 2019; published 22 March 2019)

Almost all thermal metamaterials are essentially achieved by tailoring asymmetric interaction between matrices and embedded particles. However, the asymmetric interaction results in the noncommutability of matrices and particles, which may reduce the flexibility for heat management. To solve this problem, here we propose a different mechanism by tailoring symmetric interaction between particles arranged in periodic lattices, thus called “periodic interparticle interaction.” For practical application, we refer to the representative thermal transparency, which, however, is realized by tailoring periodic interparticle interaction. Theoretical analysis, finite-element simulations, and laboratory experiments all validate the proposed mechanism. Moreover, we reunderstand the Maxwell-Garnett theory and the Bruggeman theory from their scope and relation by using theoretical analysis and finite-element analysis. Compared with the existing thermal transparency, our scheme is more feasible to handle many-particle systems. This work opens a gateway to exploring periodic interparticle interaction, and further work can be expected: (i) exploring periodic interparticle interaction with different lattice types and relative positions for particle arrangement; (ii) applying periodic interparticle interaction to achieve other functions, such as thermal camouflage.

DOI: [10.1103/PhysRevApplied.11.034056](https://doi.org/10.1103/PhysRevApplied.11.034056)

### I. INTRODUCTION

Thermal metamaterials have attracted wide research interest since 2008 [1–3]. The related mechanism is mainly to tailor asymmetric interaction between matrices and embedded particles. For example, thermal transparency in Refs. [4–7] considers the asymmetric interaction between the shell and the inside core; thermal invisibility in Refs. [8,9] tailors the asymmetric interaction between the matrix and inside particles. The two phenomena feature the same thermal conductivities between the device and the background. For the core-shell structure, the background is the region outside the shell; for the matrix plus inside particles, the background is the region outside the matrix. Therefore, the background can generally be regarded as the region excluding the device (say, the designed structure). The background may also possess uniform microstructures. Other thermal metamaterials for heat management, such as thermal cloaks [1,2,10–14], thermal concentrators [10,15,16], and thermal camouflage [17–23], are all in the framework of asymmetric interaction. Although asymmetric interaction has been well manipulated, the noncommutability of matrices and inside particles may restrict the flexibility for heat management.

To solve this problem, here we reveal the mechanism of symmetric interaction between periodic particles; say, periodic interparticle interaction. For practical application,

we take the representative thermal transparency in Refs. [4–7] as an example, but realize the phenomenon beyond the asymmetric interaction between the shell and the inside core (an equivalent expression is the neutral inclusion that was presented in Ref. [4]). Instead, we carefully tailor periodic interparticle interaction to remove the influence of periodic particles [say, particles A and particles B in Fig. 1(a)] on the background; thus, thermal transparency is also achieved. Here particles A and particles B are the designed structure, and thus the background is the region excluding particles A and particles B. If the background is a pure material, it is just the matrix where particles A and particles B are embedded. If the background possesses microstructures, it can be regarded as the matrix plus microstructures. Then the scheme will be validated by theoretical analysis, finite-element simulations, and laboratory experiments.

Moreover, we find that the formula describing periodic interparticle interaction is mathematically the same as the well-known Bruggeman formula. Although the Bruggeman formula can indeed explain symmetric interaction, the understanding is completely different in our work, which is discussed as well.

### II. THEORY FOR PERIODIC INTERPARTICLE INTERACTION

Let us start by considering the two-dimensional periodic composite material presented in Fig. 1(a). Two

\*jphuang@fudan.edu.cn

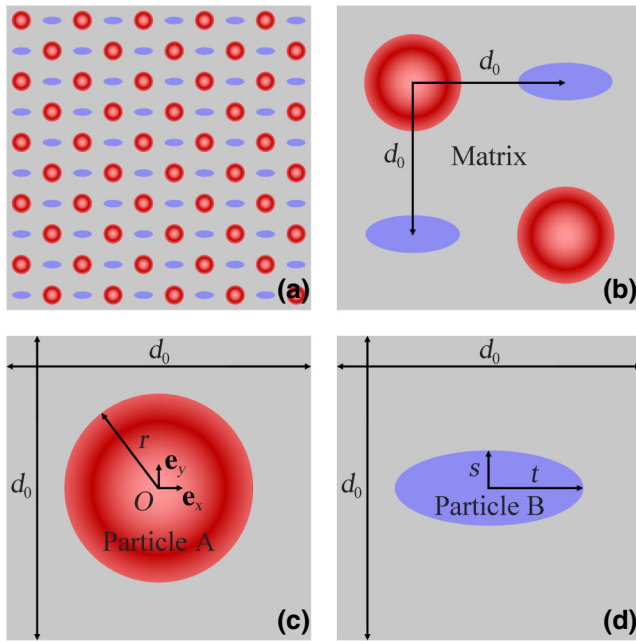


FIG. 1. (a) Periodic composite material and (b)–(d) basic structures.

types of particles are alternately embedded in the matrix with distance  $d_0$ ; see Fig. 1(b). Particle A has material anisotropy and geometry isotropy (a red graded circle with radius  $r$ ), whereas particle B is characterized by material isotropy and geometry anisotropy (a blue ellipse with semiminor axis  $s$  and semimajor axis  $t$ ); see Figs. 1(c) and 1(d). We set the thermal conductivities of particle A, particle B, and the matrix to be  $\overset{\leftrightarrow}{\kappa}_a = \text{diag}(\kappa_{\rho\rho}, \kappa_{\theta\theta})$ ,  $\kappa_b$ , and  $\kappa_m$ , respectively.  $\overset{\leftrightarrow}{\kappa}_a$  is written in the cylindrical coordinates  $(\rho, \theta)$ , whose origin is at the center of particle A. In what follows, we focus on the horizontal properties of the periodic composite material except for additional statements. In the presence of a thermal field  $E_0$  (defined as a negative temperature gradient) along the horizontal direction, the effective thermal conductivity of the periodic composite material  $\kappa_e$  can be calculated by Fourier's law:

$$\kappa_e = \frac{\langle J \rangle}{\langle E \rangle}, \quad (1)$$

where  $J$  and  $E$  represent the heat flux and the thermal field in the periodic composite material, respectively. In Eq. (1),  $\langle \dots \rangle$  denotes the area average over the whole region. Considering the local heat fluxes (and local thermal fields) in particles A  $J_a$  ( $E_a$ ), particles B  $J_b$  ( $E_b$ ), and matrix  $J_m$  ( $E_m$ ), we can rewrite Eq. (1) as

$$\kappa_e = \frac{p_a \langle J_a \rangle + p_b \langle J_b \rangle + p_m \langle J_m \rangle}{p_a \langle E_a \rangle + p_b \langle E_b \rangle + p_m \langle E_m \rangle}, \quad (2)$$

where  $p_a [= \pi r^2 / (2d_0^2)]$ ,  $p_b [= \pi st / (2d_0^2)]$ , and  $p_m = 1 - p_a - p_b$  are the area fraction of particles A, particles B, and the matrix, respectively.

Then we need to calculate the average heat fluxes  $\langle J_a \rangle$ ,  $\langle J_b \rangle$ , and  $\langle J_m \rangle$  in Eq. (2). Because of translation invariance, the calculations can be simplified to the two basic structures presented in Figs. 1(c) and 1(d). Although the matrix in Figs. 1(c) and 1(d) is finite with size  $d_0 \times d_0$ , we can still make a reasonable and contributing approximation that the matrix is infinite when the particles are small enough. The influence of the infinite-matrix approximation is analyzed after the theory for periodic interparticle interaction is established.

We first calculate the average heat flux in particle A; see Fig. 1(c). For the infinite-matrix approximation, the temperature distribution in particle A,  $T_a$ , can be expressed as [24]

$$T_a = \frac{-2r^{1-v} E_0 \kappa_m}{v \kappa_{\rho\rho} + \kappa_m} \rho^v \cos \theta + T_0, \quad (3)$$

where  $v = \sqrt{\kappa_{\theta\theta} / \kappa_{\rho\rho}}$ , and  $T_0$  is a constant temperature. The average heat flux in particle A can be calculated by

$$\langle J_a \rangle = \frac{\iint_{\Sigma} \hat{\mathbf{e}}_x \cdot (\overset{\leftrightarrow}{\kappa}_a \mathbf{E}_a) dS}{\iint_{\Sigma} dS} = \frac{\iint_{\Sigma} (\kappa_{xx} E_{ax} + \kappa_{xy} E_{ay}) dS}{\iint_{\Sigma} dS}, \quad (4)$$

where  $\hat{\mathbf{e}}_x$  is the horizontal unit vector and  $\Sigma$  represents the closed integration area (i.e., particle A),  $\kappa_{xx} = \kappa_{\rho\rho} \cos^2 \theta + \kappa_{\theta\theta} \sin^2 \theta$ ,  $\kappa_{xy} = (\kappa_{\rho\rho} - \kappa_{\theta\theta}) \sin \theta \cos \theta$ ,  $E_{ax} = -\partial T_a / \partial x$ , and  $E_{ay} = -\partial T_a / \partial y$ . After performing the integration, we can reduce Eq. (4) to

$$\langle J_a \rangle = \kappa_a \langle E_a \rangle = v \kappa_{\rho\rho} \frac{2E_0 \kappa_m}{v \kappa_{\rho\rho} + \kappa_m}, \quad (5)$$

where  $\kappa_a (= v \kappa_{\rho\rho})$  is the effective scalar thermal conductivity of particle A with the tensorial  $\overset{\leftrightarrow}{\kappa}_a$ . In what follows, we use  $\kappa_a$  if  $\overset{\leftrightarrow}{\kappa}_a$  is not necessary.

Second, we calculate the average heat flux in particle B; see Fig. 1(d). For the infinite-matrix approximation, the temperature distribution in particle B,  $T_b$ , can be expressed as [25]

$$T_b = \frac{-E_0 \kappa_m}{\kappa_b L + \kappa_m (1 - L)} \rho \cos \theta + T_0, \quad (6)$$

where the horizontal shape factor  $L$  is given by

$$L = \frac{st}{2} \int_0^\infty \frac{du}{(t^2 + u) \sqrt{(s^2 + u)(t^2 + u)}}. \quad (7)$$

It is found that the thermal field in particle B is uniform, and hence the average heat flux in particle B can be directly

expressed as

$$\langle J_b \rangle = \kappa_b \langle E_b \rangle = \kappa_b \frac{E_0 \kappa_m}{\kappa_b L + \kappa_m (1 - L)}. \quad (8)$$

We finally calculate the average heat flux in the matrix, and take the matrix in Fig. 1(c) as an example. For the infinite-matrix approximation, the temperature distribution in the matrix  $T_m$  can be expressed as [24]

$$T_m = -E_0 \rho \cos \theta + \frac{r^2 E_0 (\kappa_a - \kappa_m)}{\kappa_a + \kappa_m} \rho^{-1} \cos \theta + T_0. \quad (9)$$

The average heat flux in the matrix is then determined by

$$\langle J_m \rangle = \kappa_m \langle E_m \rangle = \kappa_m E_0, \quad (10)$$

where  $\langle E_m \rangle = E_0$  is because the effect of the term containing  $\rho^{-1}$  in Eq. (9) is local, which can be ignored because of the infinite-matrix approximation. Equation (10) can also describe the average heat flux in the matrix, as shown in Fig. 1(d).

Considering Eqs. (5), (8), and (10), we can rewrite Eq. (2) as

$$\begin{aligned} \kappa_e &= \frac{p_a \kappa_a \langle E_a \rangle + p_b \kappa_b \langle E_b \rangle + p_m \kappa_m \langle E_m \rangle}{p_a \langle E_a \rangle + p_b \langle E_b \rangle + p_m \langle E_m \rangle} \\ &= \frac{p_a \eta_a \kappa_a + p_b \eta_b \kappa_b + p_m \kappa_m}{p_a \eta_a + p_b \eta_b + p_m}, \end{aligned} \quad (11)$$

where  $\eta_a = \langle E_a \rangle / \langle E_m \rangle = 2\kappa_m / (\kappa_a + \kappa_m)$  and  $\eta_b = \langle E_b \rangle / \langle E_m \rangle = \kappa_m / [\kappa_b L + \kappa_m (1 - L)]$ . The  $\kappa_e$  determined by Eq. (11) can describe the effective thermal conductivity of the whole system composed of particles A, particles B, and the matrix. For physical understanding, Eq. (11) is, in a sense, the average of  $\kappa_a$ ,  $\kappa_b$ , and  $\kappa_m$  with respect to  $p_a \eta_a$ ,  $p_b \eta_b$ , and  $p_m$ . The weight of  $\kappa_m$  (only with  $p_m$ ) is different from the weights of  $\kappa_a$  and  $\kappa_b$ , which agrees with the comment that the interaction between the matrix and inside particles is asymmetric.

To exclude the thermal effect of the matrix, we further set  $\kappa_e$  in Eq. (11) to be  $\kappa_m$  to consider the periodic interparticle interaction between particles A and particles B, and derive the only physical solution:

$$\kappa_m = \frac{-B + \sqrt{B^2 - 4AC}}{2A}, \quad (12)$$

where  $A = p(1 - 2L) + 1$ ,  $B = -\kappa_a [p(3 - 2L) - 1] + \kappa_b [p(1 + 2L) - 1]$ ,  $C = \kappa_a \kappa_b [p(1 - 2L) - 1]$ ,  $p = p_a / p_{a+b}$ , and  $p_{a+b} = p_a + p_b$ . The  $\kappa_m$  determined by Eq. (12) can describe the periodic interparticle interaction between particles A and particles B, because the right-hand side of Eq. (12) is independent of the matrix property. In other words, particles A and particles B have the same thermal

property as the matrix determined by Eq. (12). Therefore, thermal transparency can be realized by our tailoring the periodic interparticle interaction between particles A and particles B with the aid of Eq. (12). For completeness, we present the theory for three-dimensional thermal transparency in the Appendix.

### III. VALIDATING THE INFINITE-MATRIX APPROXIMATION BY COMPARISON WITH FINITE-ELEMENT SIMULATIONS

In the process to derive Eqs. (11) and (12), we adopt the infinite-matrix approximation, which assumes that particles are small enough. So we perform finite-element simulations to analyze the influence of area fractions on predicting the effective thermal conductivities. We consider the isotropic case with  $\kappa_{\rho\rho} = \kappa_{\theta\theta}$  for particle A and  $s = t$  for particle B.  $\kappa_a$  and  $\kappa_b$  are set to be 400 and  $1 \text{ W m}^{-1} \text{ K}^{-1}$ , respectively. We compare the values of  $\kappa_e$  and  $\kappa_m$  derived from the infinite-matrix approximation [Eqs. (11) and (12)] and finite-element simulations performed with the software program COMSOL MULTIPHYSICS [26].

When discussing the influences of  $p_a$  and  $p_b$  on  $\kappa_e$ , we construct the periodic composite material with a  $5 \times 5$  array of the basic structure presented in Fig. 2(a).  $\kappa_m$  is set to be  $20 \text{ W m}^{-1} \text{ K}^{-1}$ . The solid lines in Fig. 2(a) are derived from Eq. (11), which result from the infinite-matrix approximation. Then we put the periodic composite material into a thermal field, and derive the values of  $\langle J \rangle$  and  $\langle E \rangle$  with the finite-element simulations. We further calculate  $\kappa_e$  with  $\langle J \rangle / \langle E \rangle$ , and the results are represented by the symbols in Fig. 2(a). The maximum value of  $p_a$  (and  $p_b$ ) is  $\pi/8$  (approximately 0.39), for a circle cannot fill the whole square. Clearly, the infinite-matrix approximation underestimates the effect of particle A (high thermal conductivity of  $400 \text{ W m}^{-1} \text{ K}^{-1}$ ) by about 5.8% at  $p_a = 0.39$  and overestimates the effect of particle B (low thermal conductivity of  $1 \text{ W m}^{-1} \text{ K}^{-1}$ ) by about 6.2% at  $p_b = 0.39$ .

The results shown in Fig. 2(a) illustrate that the infinite-matrix approximation is still contributing in spite of the large area fractions. The main reason is that the large area fractions (against the infinite-matrix approximation) do change the theoretically predicted temperature distributions  $T_a$ ,  $T_b$ , and  $T_m$  [Eqs. (3), (6), and (9)], but we focus only on their average effects when calculating the average heat fluxes  $\langle J_a \rangle$ ,  $\langle J_b \rangle$ , and  $\langle J_m \rangle$  [Eqs. (5), (8), and (10)]. As a result, the influence of large area fractions is reduced.

We now discuss the influence of  $p$  and  $p_{a+b}$  on  $\kappa_m$ ; see Fig. 2(b). We construct periodic particles with a  $5 \times 5$  array of the basic structure. The solid lines in Fig. 2(b) are derived from Eq. (12) (infinite-matrix approximation). We put these periodic particles into the matrix determined by Eq. (12) to analyze the practical  $\kappa_m$ . We derive the average

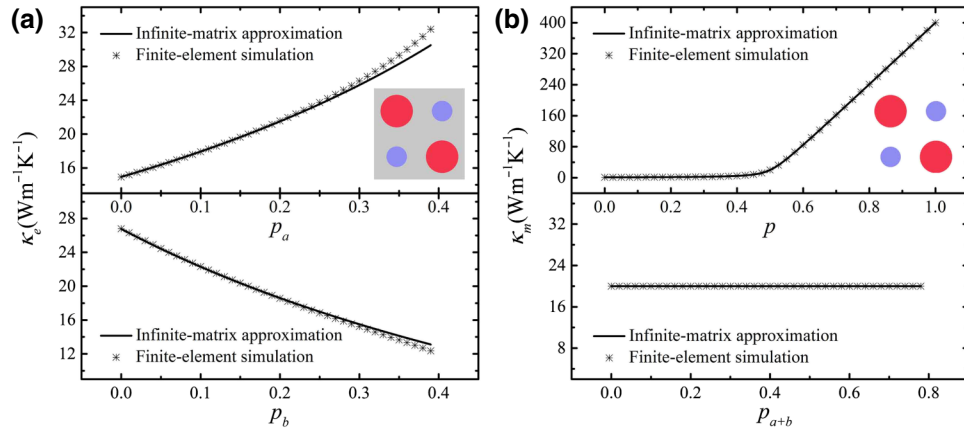


FIG. 2. Thermal conductivities of (a) periodic composite material  $\kappa_e$  and (b) periodic interparticle interaction  $\kappa_m$ , which are both given as a function of the area fraction of the particles. The solid lines in (a) [(b)] are derived from Eq. (11) [Eq. (12)], and the symbols are obtained with finite-element simulations. The size of the periodic composite material is  $10 \times 10 \text{ cm}^2$ ,  $d_0 = 1 \text{ cm}$ ,  $\kappa_a = 400 \text{ W m}^{-1} \text{K}^{-1}$ , and  $\kappa_b = 1 \text{ W m}^{-1} \text{K}^{-1}$ . Other parameters are as follows: (a)  $\kappa_m = 20 \text{ W m}^{-1} \text{K}^{-1}$ ,  $p_b = 0.16$  for the  $\kappa_e$ - $p_b$  curve, and  $p_a = 0.16$  for the  $\kappa_e$ - $p_a$  curve; (b)  $p_{a+b} = 0.24$  for the  $\kappa_m$ - $p$  curve and  $p = 0.5$  for the  $\kappa_m$ - $p_{a+b}$  curve. The symbols are derived by our putting the periodic particles into the matrix determined by Eq. (12) and calculating  $\kappa_m$  with  $\langle J_{a+b} \rangle / \langle E_{a+b} \rangle$ .

heat flux  $\langle J_{a+b} \rangle$  and average thermal field  $\langle E_{a+b} \rangle$  in particles A and particles B with the finite-element simulations. We further calculate  $\kappa_m$  with  $\langle J_{a+b} \rangle / \langle E_{a+b} \rangle$ ; the results are represented by the symbols in Fig. 2(b). The value of  $p$  ranges from 0 to 1, for it describes the relative area fraction of particles A with particles B. The maximum value of  $p_{a+b}$  is  $\pi/4$  (approximately 0.79), for a circle cannot fill the whole square. Again, the infinite-matrix approximation is well behaved with both  $p$  ranging from 0 to 1 and  $p_{a+b}$  ranging from 0 to 0.79. An intuitive reason is that the underestimation of high thermal conductivity and the overestimation of low thermal conductivity, as discussed for Fig. 2(a), cancel each other out when particles are large (e.g.,  $p_{a+b} = 0.79$ ).

On the basis of the results in Fig. 2, we feel it necessary to runderstand the two famous effective-medium theories; that is, the Maxwell-Garnett formula and the Bruggeman formula. In terms of mathematical form, Eq. (11) is the generalized Maxwell-Garnett formula [27] and Eq. (12) is the generalized Bruggeman formula [28], if we consider particle anisotropy. However, in this work, the understanding of Eqs. (11) and (12) is totally different from the previous opinions [27–29] from three perspectives.

(a) Random versus periodic: It is accepted that the two formulas can explain only completely random systems. However, the results in Fig. 2 illustrate that they are also well behaved in explaining periodic systems.

(b) Small versus big: The Maxwell-Garnett formula is thought to be applicable only when particles are small enough. However, the results in Fig. 2(a) demonstrate that the Maxwell-Garnett formula is still contributing when particles are big.

(c) Independent versus dependent: The two formulas are believed to be independent in describing different systems. However, we unify the two formulas that were previously thought to be independent, and clarify that the Bruggeman formula may be a direct result of the Maxwell-Garnett formula; that is, from Eq. (11) to Eq. (12).

Anyway, periodicity is the key to understand these results. On one hand, it helps to simplify the calculations to the two basic structures presented in Figs. 1(c) and 1(d). On the other hand, it avoids the overlap between particles, especially when area fractions are larger.

#### IV. FINITE-ELEMENT SIMULATIONS AND LABORATORY EXPERIMENTS FOR THERMAL TRANSPARENCY

We are now in a position to present the finite-element simulations and laboratory experiments for thermal transparency by tailoring the periodic interparticle interaction between particles A and particles B with Eq. (12).

Figure 3 shows the results of finite-element simulations of thermal transparency. The thermal conductivity of the region excluding particles A and particles B is set as required by Eq. (12). When we put only particles A into the background, high thermal conductivity repels isotherms; see Fig. 3(a). When we put only particles B into the background, low thermal conductivity attracts isotherms; see Fig. 3(b). When we put both particles A and particles B into the background, thermal transparency is achieved with the periodic interparticle interaction between particles A and particles B; see Fig. 3(c). The heat fluxes on the solid black lines,  $J_s$ , in Figs. 3(a)–3(c) are presented in

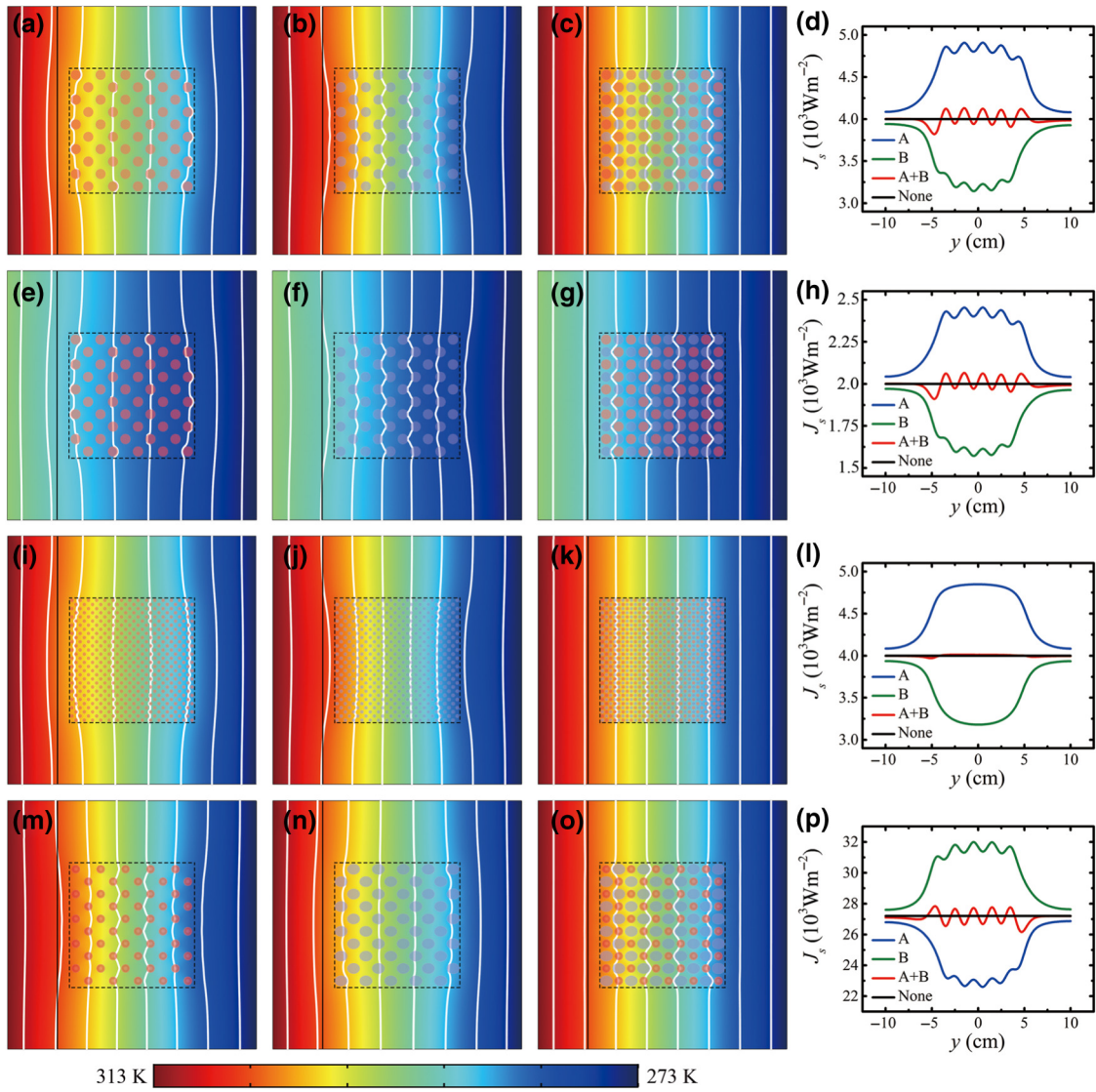


FIG. 3. Finite-element simulations of thermal transparency for (a)–(d), (e)–(h), (i)–(l) isotropic cases and (m)–(p) anisotropic cases.  $\kappa_m$  is set as required by Eq. (12). The size of the simulation box is  $20 \times 20 \text{ cm}^2$ , and that of the periodic composite material is  $10 \times 10 \text{ cm}^2$ . The solid line is located at  $x = -6 \text{ cm}$ , and the origin is located in the center of the simulation box. White lines represent isotherms. All particles are presented with 50% opacity in simulation boxes (the particle color does not correspond to temperature). Blue, green, red, and black lines in (d), (h), (l), (p) are the results with only particles A, only particles B, particles A plus particles B, and no particles, respectively. The thermal gradients in (a)–(d), (i)–(l), (m)–(p) and in (e)–(h) are 2 and  $1 \text{ K cm}^{-1}$ , respectively. Other parameters are as follows: (a)–(d)  $d_0 = 1 \text{ cm}$ ,  $\kappa_a = 400 \text{ W m}^{-1} \text{ K}^{-1}$ ,  $\kappa_b = 1 \text{ W m}^{-1} \text{ K}^{-1}$ ,  $p_a = 0.25$ ,  $p_b = 0.25$ , and  $\kappa_m = 20 \text{ W m}^{-1} \text{ K}^{-1}$ ; (e–h) the same as for (a)–(d) except for the thermal gradient; (i)–(l) the same as for (a)–(d) except for  $d_0 = 1/3 \text{ cm}$ ; (m)–(p)  $d_0 = 1 \text{ cm}$ ,  $\vec{\kappa}_a = \text{diag}(2, 0.5) \text{ W m}^{-1} \text{ K}^{-1}$ ,  $\kappa_b = 400 \text{ W m}^{-1} \text{ K}^{-1}$ ,  $p_a = 0.18$ ,  $p_b = 0.34$ ,  $t/s = 1.2$ , and  $\kappa_m = 136 \text{ W m}^{-1} \text{ K}^{-1}$ .

Fig. 3(d). The red line (with some fluctuation) echoes with the black line in Fig. 3(d), which validates the existence of thermal transparency. Then we change only the thermal gradient; see Figs. 3(e)–3(g). The shapes of the isotherms are exactly the same as those in Figs. 3(a)–3(c), although the concrete temperature and heat flux [Fig. 3(h)] are different. The thermal gradient can be any value because the thermal property determined by Eq. (12) is independent of the thermal gradient. We further change the

value of parameter  $d_0$  and keep the values of the other parameters unchanged; see Figs. 3(i)–3(l). The results are basically the same as those in Figs. 3(a)–3(d), but with smaller fluctuation. Therefore,  $d_0$  does not affect  $\kappa_m$  predicted by Eq. (12), but affects fluctuation. Finally, we discuss an anisotropic case with material anisotropy of particle A and geometry anisotropy of particle B; see Figs. 3(m)–3(p). Anisotropic particle A with low thermal conductivity attracts isotherms, whereas anisotropic

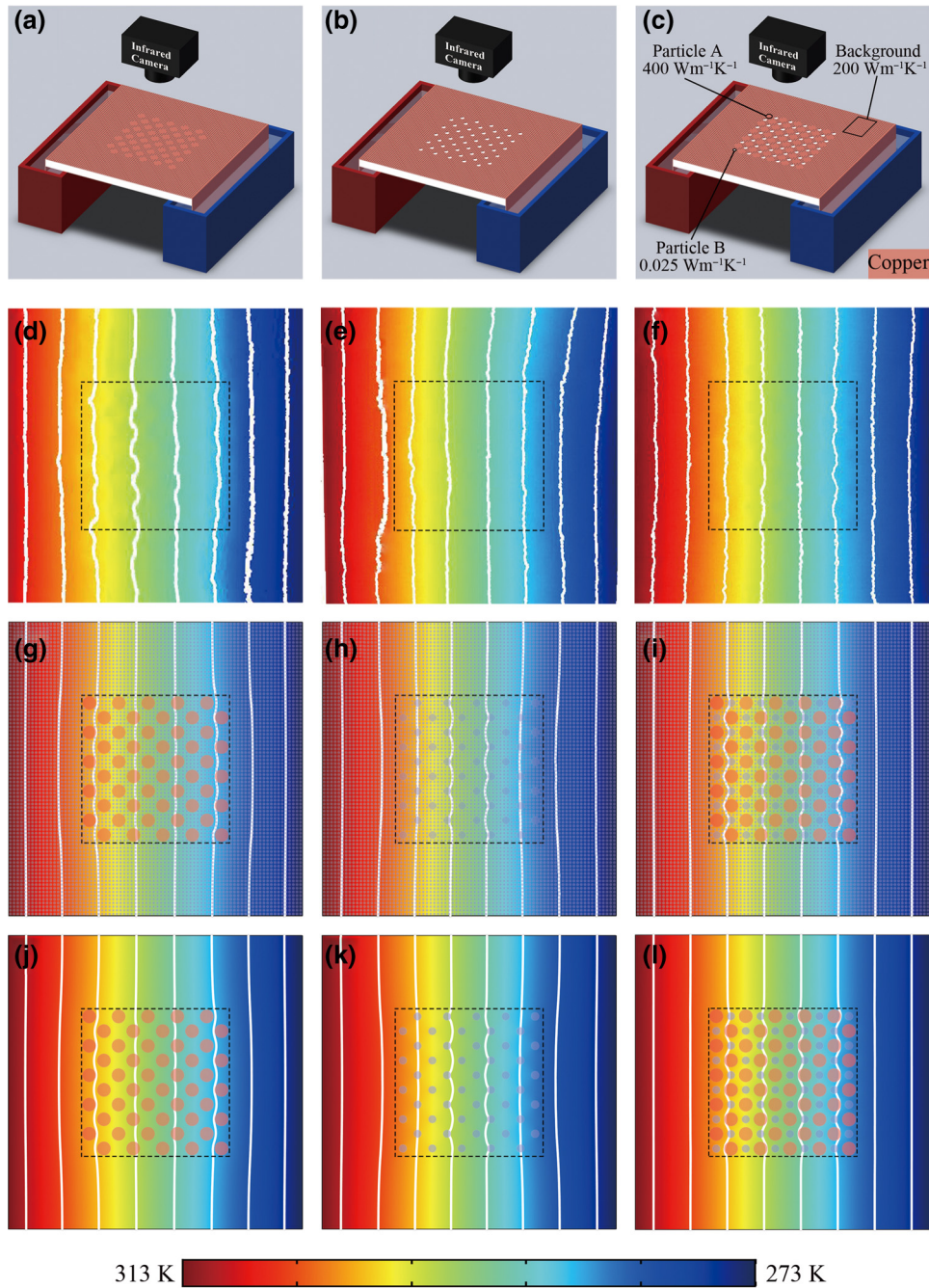


FIG. 4. Laboratory experiments for thermal transparency for (a)–(c) three samples, (d)–(f) measured results, (g)–(i) corresponding results of finite-element simulations, and (j)–(l) results of finite-element simulations by our directly setting  $\kappa_m = 200 \text{ W m}^{-1} \text{ K}^{-1}$ . The sample size is  $20 \times 20 \text{ cm}^2$ , and the size of the periodic composite material is  $10 \times 10 \text{ cm}^2$ . Hot and cold baths are set at 313 and 273 K, respectively. The thermal conductivities of copper and air are 400 and  $0.025 \text{ W m}^{-1} \text{ K}^{-1}$ , respectively.  $\kappa_a = 400 \text{ W m}^{-1} \text{ K}^{-1}$ ,  $\kappa_b = 0.025 \text{ W m}^{-1} \text{ K}^{-1}$ ,  $d_0 = 1 \text{ cm}$ ,  $p_a = 0.33$ , and  $p_b = 0.11$ . The area fraction of air holes (excluding particles A and particles B) in (a)–(c) is 0.33, and the distance between these air holes is 0.25 cm. All particles are presented with 50% opacity in simulation boxes except for experimental results (the particle color does not correspond to temperature).

particle B with high thermal conductivity repels isotherms. Thermal transparency is still obtained when particles A and particles B are put together; see Fig. 3(o). Hence, the red line (with some fluctuation) agrees with the black line as shown in Fig. 3(p).

Figure 4 shows the results of the laboratory experiments for thermal transparency. For experimental realization,  $\kappa_a$ ,  $\kappa_b$ , and  $\kappa_m$  are three related thermal conductivities, which are all set to be isotropic for feasibility. We use copper and air as the material of particle A and particle B, respectively.

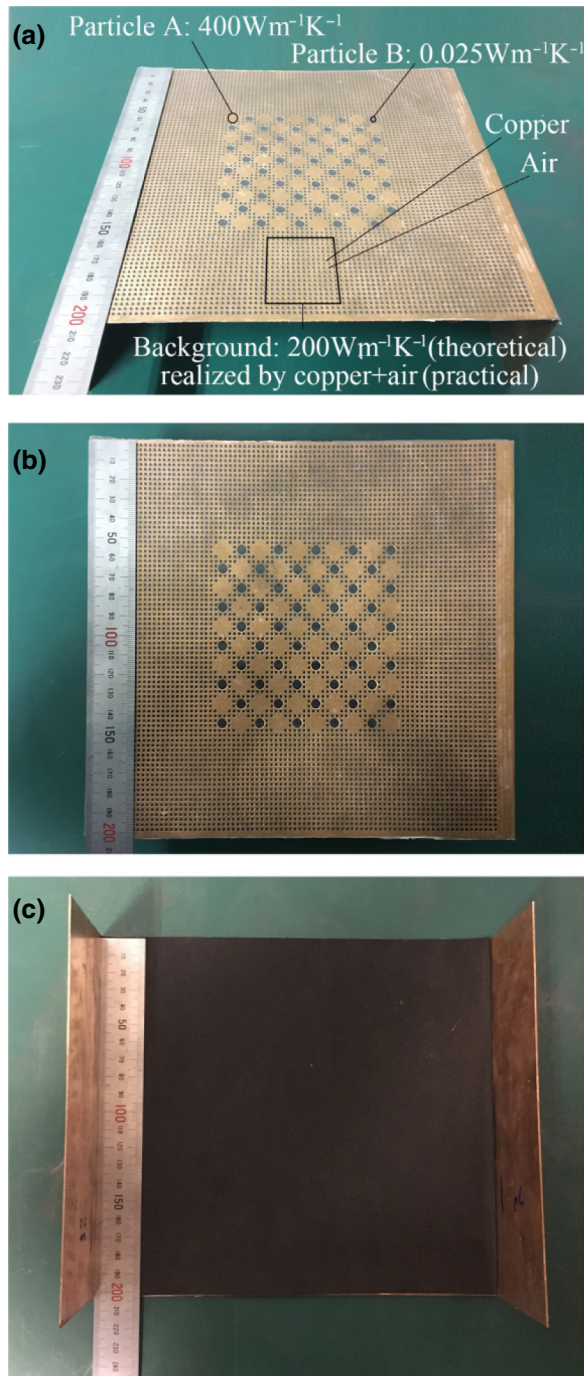


FIG. 5. Real product of Fig. 4(c) with (a) side view, (b) top view, and (c) bottom view.

$\kappa_m$  is determined by Eq. (12), and is realized by our carving air holes in a copper plate with effective-medium theory [8]. Therefore, we use only two materials (copper and air) to realize three thermal conductivities ( $\kappa_a$ ,  $\kappa_b$ , and  $\kappa_m$ ). The background possesses microstructures and is composed of copper (matrix) and air holes (microstructures) with area fraction 0.33. The three samples are fabricated by laser cutting, and are measured between hot and cold baths with

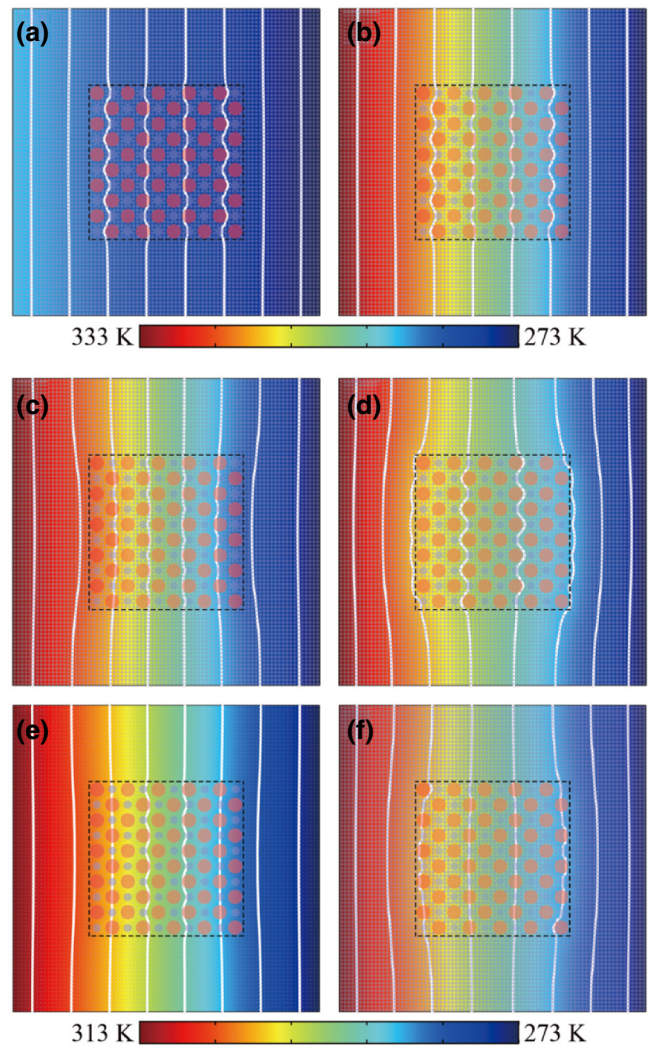


FIG. 6. Simulation results for other conditions. The parameters are the same as those for Fig. 4(i) except for (a) the thermal gradient is  $1 \text{ K cm}^{-1}$ , for (b) the thermal gradient is  $3 \text{ K cm}^{-1}$ , for (c) the matrix thermal conductivity is  $1000 \text{ W m}^{-1} \text{ K}^{-1}$ , for (d) the matrix thermal conductivity is  $100 \text{ W m}^{-1} \text{ K}^{-1}$ , for (e) the area fraction of the voids is 0.05, and for (f) the area fraction of the voids is 0.66.

an infrared camera (FLIR E60); see Figs. 4(a)–4(c). The upper and lower surfaces are, respectively, covered with transparent plastic and foamed plastic (both insulated) to reduce the influence of infrared reflection and thermal convection. A real product of Fig. 4(c) is presented in the Appendix; see Fig. 5. The measured results are presented in Figs. 4(d)–4(f). We also perform finite-element simulations based on the three samples; the results are presented in Figs. 4(g)–4(i).

Moreover, we directly set  $\kappa_m = 200 \text{ W m}^{-1} \text{ K}^{-1}$  to perform simulations, rather than the structure of a copper plate with air holes carved in it; the corresponding results are presented in Figs. 4(j)–4(l). The accordance between the

results of the laboratory experiments [Figs. 4(d)–4(f)] and the results of the finite-element simulations [Figs. 4(g)–4(i) or Figs. 4(j)–4(l)] validates the scheme of tailoring periodic interparticle interaction to achieve thermal transparency.

According to the results presented Fig. 4(i), we also change the thermal gradient, matrix thermal conductivity, and matrix area fraction to study the changes of thermal transparency (particles A and particles B are kept unchanged). The results are presented in the Appendix; see Fig. 6. We conclude that the thermal gradient will not affect thermal transparency but matrix properties will affect it. The physical understanding is that the dominant Eq. (12) is independent of the thermal gradient but is dependent on the matrix properties.

## V. DISCUSSION AND CONCLUSION

In this work, we investigate the periodic interparticle interaction between particles A and particles B, which are commutable. However, this is just a beginning for exploring periodic interparticle interaction, and deeper mechanisms remain to be studied, at least from two aspects:

(a) Lattice type: Here we arrange the particles with the simplest square lattice; see Fig. 1(a). A question is how to calculate other lattice types. For example, a rectangle lattice is certain to result in anisotropy compared with a square lattice, let alone the more-complicated orthorhombic lattice.

(b) Relative position: Here the particles are alternately arranged along both the horizontal direction and the vertical direction; see Fig. 1(a). A question is how to calculate other relative positions. For example, if the particles are alternately arranged along only the horizontal direction, the new relative position will also result in anisotropy.

In summary, we propose a distinct mechanism for achieving thermal transparency that is induced by the symmetric interaction between periodic particles (namely, periodic interparticle interaction) rather than neutral inclusions [4]. Theoretical analysis, finite-element simulations, and laboratory experiments all validate the proposed mechanism. Moreover, we runderstand the Maxwell-Garnett formula and the Bruggeman formula from three aspects. That is, the two formulas can explain (i) periodic systems (ii) with large area fractions of particles, and (iii) they depend on each other. Our mechanism is feasible to handle many-particle systems for removing thermal stress concentration, preventing infrared detection, etc. On the same footing, periodic interparticle interaction proposed in this work can also be extended to realize other functions, such as thermal camouflaging.

## ACKNOWLEDGMENT

We acknowledge financial support by the National Natural Science Foundation of China under Grant No. 11725521.

## APPENDIX

To realize the three-dimensional thermal transparency, Eqs. (5), (8), and (10) correspondingly become

$$\langle J'_a \rangle = \kappa'_a \langle E'_a \rangle = v' \kappa'_{\rho\rho} \frac{3E'_0 \kappa'_m}{v' \kappa'_{\rho\rho} + 2\kappa'_m}, \quad (\text{A1})$$

$$\langle J'_b \rangle = \kappa'_b \langle E'_b \rangle = \kappa'_b \frac{E'_0 \kappa'_m}{\kappa'_b L' + \kappa'_m (1 - L')}, \quad (\text{A2})$$

$$\langle J'_m \rangle = \kappa'_m \langle E'_m \rangle = \kappa'_m E'_0, \quad (\text{A3})$$

where the primes represent the case of three dimensions,  $\kappa'_a (= v' \kappa'_{\rho\rho})$  is the effective scalar thermal conductivity of the particle with tensorial  $\overset{\leftarrow}{\kappa}'_a [= \text{diag}(\kappa'_{\rho\rho}, \kappa'_{\theta\theta}, \kappa'_{\varphi\varphi})]$  with  $\kappa'_{\theta\theta} = \kappa'_{\varphi\varphi}$ , and  $v' = -1/2 + \sqrt{1/4 + 2\kappa'_{\theta\theta}/\kappa'_{\rho\rho}}$ . The horizontal shape factor  $L'$  can be calculated by

$$L' = \frac{s't'w'}{2} \int_0^\infty \frac{du}{(t'^2 + u) \sqrt{(s'^2 + u)(t'^2 + u)(w'^2 + u)}}, \quad (\text{A4})$$

where  $w'$  is the third semiaxis of the ellipsoid.

Owing to Eqs. (A1)–(A3), Eqs. (11) and (12) should, respectively, become

$$\begin{aligned} \kappa'_e &= \frac{p'_a \kappa'_a \langle E'_a \rangle + p'_b \kappa'_b \langle E'_b \rangle + p'_m \kappa'_m \langle E'_m \rangle}{p'_a \langle E'_a \rangle + p'_b \langle E'_b \rangle + p'_m \langle E'_m \rangle} \\ &= \frac{p'_a \eta'_a \kappa'_a + p'_b \eta'_b \kappa'_b + p'_m \kappa'_m}{p'_a \eta'_a + p'_b \eta'_b + p'_m}, \end{aligned} \quad (\text{A5})$$

$$\kappa'_m = \frac{-B' + \sqrt{B'^2 - 4A'C'}}{2A'}, \quad (\text{A6})$$

where  $p'_a = 2\pi r^3/3d_0^3$ ,  $p'_b = 2\pi s't'w'/3d_0^3$ ,  $p'_m = 1 - p'_a - p'_b$ ,  $\eta'_a = \langle E'_a \rangle / \langle E'_m \rangle = 3\kappa'_m / (\kappa'_a + 2\kappa'_m)$ ,  $\eta'_b = \langle E'_b \rangle / \langle E'_m \rangle = \kappa'_m / [\kappa'_b L' + \kappa'_m (1 - L')]$ ,  $A' = p' (1 - 3L') + 2$ ,  $B' = -\kappa'_a [p' (4 - 3L') - 1] + \kappa'_b [p' (2 + 3L') - 2]$ ,  $C' = \kappa'_a \kappa'_b [p' (1 - 3L') - 1]$ , and  $p' = p'_a / (p'_a + p'_b)$ .  $\kappa'_m$  determined by Eq. (A6) can describe the three-dimensional periodic interparticle interaction, because the right-hand side of Eq. (A6) is independent of the matrix property.



The real product of Fig. 4(c) is shown in Fig. 5.

According to the result in Fig. 4(i), we keep particles A and particles B unchanged, and change the thermal gradient and matrix properties to study the changes of thermal transparency. We change the thermal gradient to be  $1 \text{ K cm}^{-1}$  [Fig. 6(a)] and  $3 \text{ K cm}^{-1}$  [Fig. 6(b)], and thermal transparency remains unchanged. We change the matrix thermal conductivity from  $400 \text{ W m}^{-1} \text{ K}^{-1}$  [Fig. 6(c)] and  $100 \text{ W m}^{-1} \text{ K}^{-1}$  [Fig. 6(d)]. The isotherms are attracted and repelled, respectively. Finally, we change the area fraction of the voids from 0.33 to 0.05 [Fig. 6(e)] and 0.66 [Fig. 6(f)]. The isotherms are also attracted and repelled, respectively.

- 
- [1] C. Z. Fan, Y. Gao, and J. P. Huang, Shaped graded materials with an apparent negative thermal conductivity, *Appl. Phys. Lett.* **92**, 251907 (2008).
- [2] T. Y. Chen, C. N. Weng, and J. S. Chen, Cloak for curvilinearly anisotropic media in conduction, *Appl. Phys. Lett.* **93**, 114103 (2008).
- [3] M. Maldovan, Sound and heat revolutions in phononics, *Nature* **503**, 209 (2013).
- [4] X. He, and L. Z. Wu, Thermal transparency with the concept of neutral inclusion, *Phys. Rev. E* **88**, 033201 (2013).
- [5] L. W. Zeng, and R. X. Song, Experimental observation of heat transparency, *Appl. Phys. Lett.* **104**, 201905 (2014).
- [6] T. Z. Yang, X. Bai, D. L. Gao, L. Z. Wu, B. W. Li, J. T. L. Thong, and C. W. Qiu, Invisible sensors: Simultaneous sensing and camouflaging in multiphysical fields, *Adv. Mater.* **27**, 7752 (2015).
- [7] R. Z. Wang, L. J. Xu, Q. Ji, and J. P. Huang, A thermal theory for unifying and designing transparency, concentrating and cloaking, *J. Appl. Phys.* **123**, 115117 (2018).
- [8] L. J. Xu, C. R. Jiang, J. Shang, R. Z. Wang, and J. P. Huang, Periodic composites: Quasi-uniform heat conduction, Janus thermal illusion, and illusion thermal diodes, *Eur. Phys. J. B* **90**, 221 (2017).
- [9] J. Shang, C. R. Jiang, L. J. Xu, and J. P. Huang, Many-particle thermal invisibility and diode from effective media, *J. Heat Transfer* **140**, 092004 (2018).
- [10] S. Narayana, and Y. Sato, Heat Flux Manipulation with Engineered Thermal Materials, *Phys. Rev. Lett.* **108**, 214303 (2012).
- [11] R. Schittny, M. Kadic, S. Guenneau, and M. Wegener, Experiments on Transformation Thermodynamics: Molding the Flow of Heat, *Phys. Rev. Lett.* **110**, 195901 (2013).
- [12] H. Y. Xu, X. H. Shi, F. Gao, H. D. Sun, and B. L. Zhang, Ultrathin Three-dimensional Thermal Cloak, *Phys. Rev. Lett.* **112**, 054301 (2014).
- [13] T. C. Han, X. Bai, D. L. Gao, J. T. L. Thong, B. W. Li, and C. W. Qiu, Experimental Demonstration of a Bilayer Thermal Cloak, *Phys. Rev. Lett.* **112**, 054302 (2014).
- [14] Y. G. Ma, Y. C. Liu, M. Raza, Y. D. Wang, and S. L. He, Experimental Demonstration of a Multiphysics Cloak: Manipulating Heat Flux and Electric Current Simultaneously, *Phys. Rev. Lett.* **113**, 205501 (2014).
- [15] R. S. Kapadia, and P. R. Bandaru, Heat flux concentration through polymeric thermal lenses, *Appl. Phys. Lett.* **105**, 233903 (2014).
- [16] L. J. Xu, S. Yang, and J. P. Huang, Thermal theory for heterogeneously architected structure: Fundamentals and application, *Phys. Rev. E* **98**, 052128 (2018).
- [17] T. C. Han, X. Bai, J. T. L. Thong, B. W. Li, and C. W. Qiu, Full control and manipulation of heat signatures: Cloaking, camouflage and thermal metamaterials, *Adv. Mater.* **26**, 1731 (2014).
- [18] X. He, and L. Z. Wu, Illusion thermodynamics: A camouflage technique changing an object into another one with arbitrary cross section, *Appl. Phys. Lett.* **105**, 221904 (2014).
- [19] T. Z. Yang, Y. Su, W. Xu, and X. D. Yang, Transient thermal camouflage and heat signature control, *Appl. Phys. Lett.* **109**, 121905 (2016).
- [20] R. Hu, S. L. Zhou, Y. Li, D. Y. Lei, X. B. Luo, and C. W. Qiu, Illusion thermotics, *Adv. Mater.* **30**, 1707237 (2018).
- [21] S. L. Zhou, R. Hu, and X. B. Luo, Thermal illusion with twinborn-like heat signatures, *Int. J. Heat Mass Transfer* **127**, 607 (2018).
- [22] L. J. Xu, R. Z. Wang, and J. P. Huang, Camouflage thermotics: A cavity without disturbing heat signatures outside, *J. Appl. Phys.* **123**, 245111 (2018).
- [23] L. J. Xu, and J. P. Huang, A transformation theory for camouflaging arbitrary heat sources, *Phys. Lett. A* **382**, 3313 (2018).
- [24] L. J. Xu, S. Yang, and J. P. Huang, Designing effective thermal conductivity of materials of core-shell structure: Theory and simulation, *Phys. Rev. E* **99**, 022107 (2019).
- [25] T. C. Han, P. Yang, Y. Li, D. Y. Lei, B. W. Li, K. Hipalgaonkar, and C. W. Qiu, Full-parameter omnidirectional thermal metadevices of anisotropic geometry, *Adv. Mater.* **30**, 1804019 (2018).
- [26] <http://www.comsol.com/>.
- [27] J. C. Maxwell Garnett, Colours in metal glasses and in metallic films, *Philos. Trans. R. Soc. Lond. Ser. A* **203**, 385 (1904).
- [28] D. A. G. Bruggeman, Calculation of various physics constants in heterogenous substances: Dielectricity constants and conductivity of mixed bodies from isotropic substances, *Ann. Phys.* **24**, 636 (1935).
- [29] M. Wang, and N. Pan, Predictions of effective physical properties of complex multiphase materials, *Mater. Sci. Eng. R* **63**, 1 (2008).